Published OnlineFirst May 26, 2021; DOI: 10.1158/0008-5472.CAN-21-0474

Spectral Endoscopy Enhances Contrast for Neoplasia in Surveillance of Barrett's Esophagus

Dale J. Waterhouse[1], Wladyslaw Januszewicz[2], Sharib Ali[3], Rebecca C. Fitzgerald[4], Massimiliano di Pietro[4], and Sarah E. Bohndiek[1]

ABSTRACT

Early detection of esophageal neoplasia enables curative endoscopic therapy, but the current diagnostic standard of care has low sensitivity because early neoplasia is often inconspicuous with conventional white-light endoscopy. Here, we hypothesized that spectral endoscopy could enhance contrast for neoplasia in surveillance of patients with Barrett's esophagus. A custom spectral endoscope was deployed in a pilot clinical study of 20 patients to capture 715 *in vivo* tissue spectra matched with gold standard diagnosis from histopathology. Spectral endoscopy was sensitive to changes in neovascularization during the progression of disease; both non-dysplastic and neoplastic Barrett's esophagus showed higher blood volume relative to healthy squamous tissue ($P = 0.001$ and 0.02, respectively), and vessel radius appeared larger in neoplasia relative to non-dysplastic Barrett's esophagus ($P = 0.06$). We further developed a deep learning algorithm capable of classifying spectra of neoplasia versus non-dysplastic Barrett's esophagus with high accuracy (84.8% accuracy, 83.7% sensitivity, 85.5% specificity, 78.3% positive predictive value, and 89.4% negative predictive value). Exploiting the newly acquired library of labeled spectra to model custom color filter sets identified a potential 12-fold enhancement in contrast between neoplasia and non-dysplastic Barrett's esophagus using application-specific color filters compared with standard-of-care white-light imaging (perceptible color difference = 32.4 and 2.7, respectively). This work demonstrates the potential of endoscopic spectral imaging to extract vascular properties in Barrett's esophagus, to classify disease stages using deep learning, and to enable high-contrast endoscopy.

Significance: The results of this pilot first-in-human clinical trial demonstrate the potential of spectral endoscopy to reveal disease-associated vascular changes and to provide high-contrast delineation of neoplasia in the esophagus.

Graphical Abstract: http://cancerres.aacrjournals.org/content/canres/81/12/3415/F1.large.jpg.

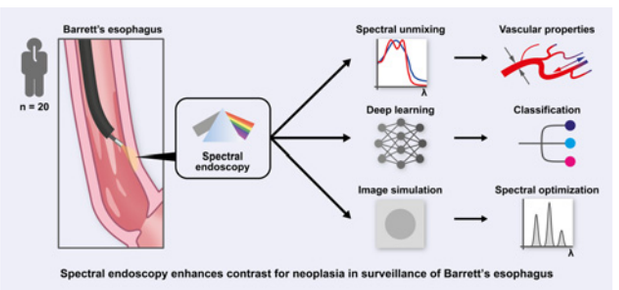

Introduction

Barrett's esophagus is an acquired condition that predisposes patients to the development of esophageal adenocarcinoma (1). Fortuitously for early detection efforts, this malignancy occurs through intermediate dysplastic stages, which can be curatively treated using endoscopic resection or ablation. Thus, patients with Barrett's esophagus undergo regular routine surveillance using high-resolution white-light endoscopy (HR-WLE) together with random tissue biopsies. Unfortunately, this has low sensitivity as dysplasia is: heterogeneous in shape and size; patchy in its distribution; and often inconspicuous on HR-WLE (2, 3).

The low sensitivity of the current standard-of-care (SOC) has motivated the development of many advanced imaging techniques based on the interactions between light and tissue (4). When light travels through tissue, it is absorbed by endogenous chromophores such as hemoglobin and scattered by endogenous structures such as organelles and cell nuclei (5). Disease-related biochemical and structural changes in the epithelial layer alter the distribution and abundance of absorbers and scatterers, resulting in subtle changes to the spectral properties of light exiting the tissue. Spectral imaging techniques aim to capture this rich endogenous contrast to reveal underlying pathology (6, 7).

HR-WLE represents a simple case of spectral imaging, where a color camera acquires a measurement of three broad color bands: Red (620 ± 40 nm), green (540 ± 40 nm), and blue (470 ± 40 nm) to replicate the spectral sensitivity of human vision (8). Though this represents a substantial improvement over monochrome imaging, finer spectral information is lost as the light is pooled into three broad bands. More recently, narrow band imaging (NBI; ref. 9) was developed to enhance contrast for vasculature, using two narrow illumination bands (415 ± 10 nm and 540 ± 10 nm). Similarly, blue-light imaging uses a narrow band of blue light (410 ± 10 nm) to improve the contrast of mucosal vasculature (10). NBI filters were selected from

[1]Department of Physics and Cancer Research UK Cambridge Institute, University of Cambridge, Cambridge, United Kingdom. [2]Department of Gastroenterology, Hepatology, and Clinical Oncology, Medical Center for Postgraduate Education, Warsaw, Poland. [3]Institute of Biomedical Engineering, University of Oxford, Oxford, United Kingdom. [4]MRC Cancer Unit, Hutchison/MRC Research Center, University of Cambridge, Cambridge, United Kingdom.

Note: Supplementary data for this article are available at Cancer Research Online (http://cancerres.aacrjournals.org/).

Corresponding Authors: Sarah E. Bohndiek, University of Cambridge, Cavendish Laboratory, Cambridge CB3 0HE, UK. Phone: 44-122-333-7267; E-mail: seb53@cam.ac.uk; and Massimiliano di Pietro, md460@mrc-cu.cam.ac.uk

Cancer Res 2021;81:3415–25

doi: 10.1158/0008-5472.CAN-21-0474

Published OnlineFirst May 26, 2021; DOI: 10.1158/0008-5472.CAN-21-0474

9 off-the-shelf filters for their ability to enhance contrast for vasculature in the human tongue (11) based on the strong absorption of light by hemoglobin at those wavelengths. Even with this relatively crude selection of only two narrow spectral filters, NBI has proven advantageous in the detection and characterization of early Barrett's esophagus–related neoplasia. It was the first advanced imaging technique to meet the American Society for Gastrointestinal Endoscopy Preservation and Incorporation of Valuable Endoscopic Innovations (PIVI; ref. 12) requirements for recommendation in Barrett's esophagus surveillance (13) and has been successfully translated into routine clinical practice, demonstrating the potential of spectral imaging to improve the SOC. Nevertheless, NBI requires a high level of operator expertise for interpretation and formal evidence that NBI improves detection of early neoplasia in Barrett's esophagus on a per-patient basis is lacking.

Capturing additional spectral information during endoscopic imaging could further augment the visualization provided to the endoscopist by NBI, for example, by measuring the spectral characteristics associated with oxy- and deoxyhemoglobin to quantitatively assess hemoglobin concentration and oxygenation within the vasculature. Furthermore, comprehensive evaluation of the spectral features of the tissue enables the application of learning-based approaches for automated interpretation or classification of disease state. Yet despite several prior studies (14–16) of diffuse reflectance spectra in Barrett's esophagus, our understanding of how such spectral information evolves with disease state and could be used assist the endoscopist during diagnostic procedures remains limited (16–18).

We hypothesized that spectral endoscopy could enhance contrast for neoplasia in surveillance of patients with Barrett's esophagus. To this end, we first created a custom spectral endoscope that captures detailed attenuation spectra and undertook a pilot clinical study to acquire *in vivo* esophageal tissue spectra matched with gold standard histopathological diagnosis of disease state. The acquired spectra were then analyzed using both model-based and learning-based methods to test our hypothesis. On the basis of our promising findings with the complete spectral information, we then simulated the formation of color images using application-specific filters comparing squamous, non-dysplastic Barrett's esophagus and neoplastic tissue types. We compared our alternative composition of color channels that were optimized on the basis of our spectral endoscopy data with SOC WLE and NBI. Our findings show that using spectral data to inform color channel selection for endoscopy has the potential to achieve up to a 12-fold contrast improvement for neoplasia within non-dysplastic Barrett's esophagus compared with current SOC.

Materials and Methods

Spectral endoscope

To measure tissue spectra *in vivo*, a custom spectral endoscope (**Fig. 1A**) was designed and constructed using an accessory channel "babyscope" (**Fig. 1B**, PolyScope, PolyDiagnost) that can be introduced through the accessory channel of a therapeutic gastroscope (**Fig. 1C**). This includes: A single fiber light guide to relay illumination from outside the patient and direct it onto the tissue; and a 10,000-fibrelet imaging bundle to relay diffusely reflected light from the esophageal tissue to custom external detection optics. Using this unmodified CE-marked device to relay light between the esophagus and external optics facilitated swift clinical translation of the spectral endoscope. In addition, the use of external optics removed the challenges associated with miniaturization of optics for chip-on-tip integration.

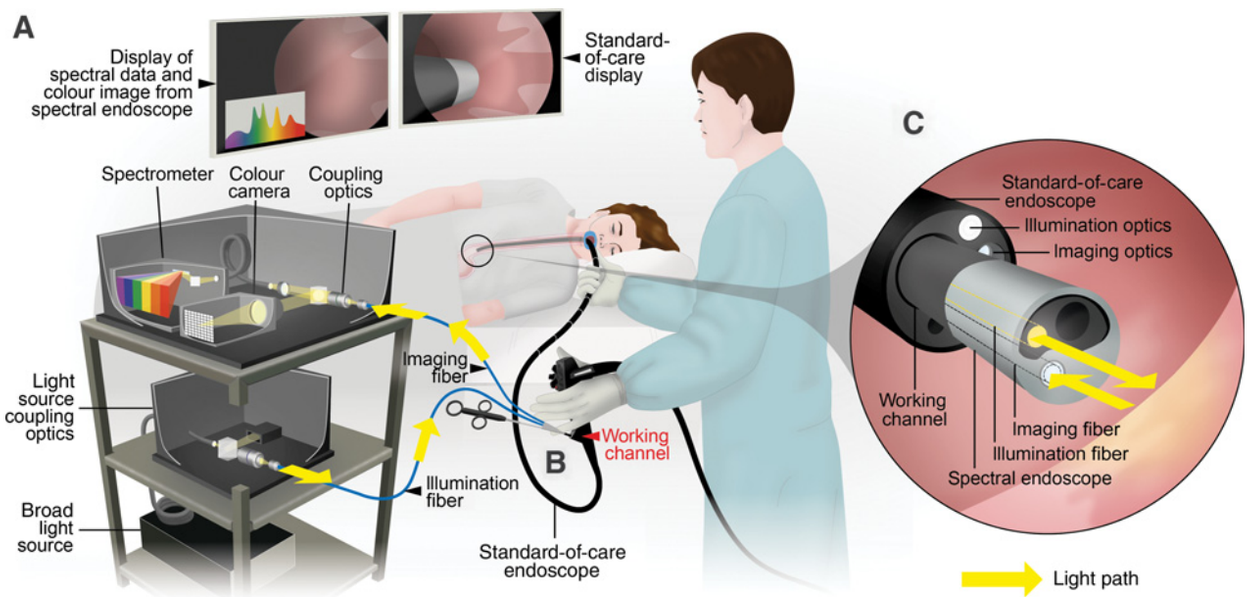

Figure 1.

Schematic overview of the spectral endoscope during operation via the working channel of the therapeutic gastroscope. **A,** Broadband illumination is coupled into the illumination fiber. Reflected light is relayed along the imaging fiber bundle, collected by an objective lens, split, and passed to either the spectrometer, to measure the diffuse tissue reflectance spectrum, or the standard color camera, to record reference images to aid positioning. All optics are safely housed inside optical enclosures. **B,** The spectral endoscope is inserted via the working channel of the therapeutic gastroscope. **C,** The spectral endoscope tip enters the esophagus through the distal tip of the therapeutic gastroscope. Light is delivered to the tissue region of interest via the illumination fiber, and reflected light is collected via the imaging fiber.

Published OnlineFirst May 26, 2021; DOI: 10.1158/0008-5472.CAN-21-0474

The babyscope was coupled to a broadband supercontinuum light source (SuperK COMPACT, NKT Photonics) that provides illumination from 450 to 850 nm. Reflected light relayed along the imaging fiber bundle was collected by an objective lens (UPLFLN20x, Olympus), split (BSN10R, Thorlabs), and focused into a spectrometer (AvaSpec-ULS2048, spectral range 200–1,100 nm, grating 300 lines/mm, slit size 50 μm, Avantes) to measure the diffuse tissue reflectance spectrum and onto a standard color camera (Grasshopper 3.0, IDS) to record reference images. The endoscope settings were controlled using an interface developed in LabVIEW (National Instruments) running on a PC and a tablet (Surface Pro, Microsoft; Supplementary Fig. S1). Using standard spectral analysis methods, the measured diffuse reflectance spectra were processed to yield tissue attenuation spectra (Supplementary Methods, Supplementary Fig. S2).

Study population and design

This prospective pilot cohort study was carried out at the Cambridge Clinical Research Centre, Cambridge University Hospitals, UK. Eligible patients were adults (at least 18 years old) with a previous diagnosis of Barrett's esophagus with an endoscopic length of at least 2 cm if circumferential (circumferential extent C≥2 according to the Prague classification; ref. 19) or at least 3 cm if not circumferential (maximal extent M≥3 according to the Prague classification). Exclusion criteria are listed in the Supplementary Materials. The trial was reviewed by Cambridgeshire Research Ethics Committee and was approved in March 2018 (18/NW/0134).

The trial was registered at ClinicalTrials.gov (NCT03388047). Initially, the primary outcome measure was to be the level of confidence in delineating the area of interest by multispectral imaging. In the first two patients it became clear that this would not be possible, due to the limited image quality of the prototype device, so the protocol was amended, with focus shifted to the initial secondary aims: (i) To assess the feasibility of imaging with the spectral endoscope, ensuring that the device could be used to capture data in a clinical environment and with minimal interruption to clinical workflow; (ii) to evaluate the spectral imaging patterns associated with non-dysplastic versus dysplastic Barrett's esophagus to build a library of diagnostically useful spectral characteristics, because these are currently unknown and not easily investigated using *ex vivo* tissue.

Between May 2018 and December 2019, a total of 20 subjects were recruited to the study (Supplementary Table S1). All patients provided written informed consent. Of these, one subject was considered unfit for endoscopic procedure due to concomitant acute comorbidity and one was excluded as the visible lesion was too small for spectral imaging. Of the 18 subjects that underwent SOC endoscopic procedures, 3 were excluded from analysis because of insufficient illumination for spectral imaging ($n = 2$) or failure of the SOC recording unit ($n = 1$).

Spectral endoscopy was performed in 15 subjects at 44 distinct regions: 9 regions of squamous tissue, 24 regions of NDBE, 7 regions of dysplasia and 4 regions of intramucosal carcinoma. Of the 35 Barrett's esophagus tissue regions, 34 were confirmed with histopathological assessment from 45 collected samples (31 biopsies, 14 endoscopic mucosal resections). One *bona fide* NDBE region was included without tissue confirmation (patient number 12) as the control region identified on endoscopy was diagnosed as dysplastic by histopathology. Co-registration between spectral imaging data and histopathological diagnosis was successful for 28 regions, yielding a total of 556 labeled spectra for analysis (**Table 1**), plus an additional 159 spectra from 9 squamous regions (Supplementary Fig. S3). The mean integration time for spectral acquisition was 170 ± 70 ms. Acquiring spectral data lengthened the overall procedure time by <10 minutes per trial (spectral data captured for mean of 5.2 ± 1.5 minutes per trial).

Endoscopic procedure and histopathology

The study design prioritized the collection of spectra matched to gold standard diagnosis from histopathology (**Fig. 2**). Each procedure was performed by a single experienced endoscopist (MdP).

i. After local anesthesia and/or conscious sedation (Midazolam ± Fentalyl) the patient was intubated with a high-resolution white-light endoscope (H290Z, Olympus). The endoscopist thoroughly cleaned the esophageal mucosa using a water jet. The endoscopist thoroughly inspected the mucosal surface of the esophagus. Cautery marks were placed around two regions of interest: One suspicious lesion and one region of Barrett's esophagus as a control (**Fig. 2A**). Cautery marks, rather than dyes, were used to create small distinct marks with no risk of staining adjacent tissue at the site of interest. In the absence of suspicious lesions, one or more random areas within the Barrett's esophagus segment were selected depending on the length of the Barrett's esophagus. The HR-WLE video stream was recorded using a recording unit (SMP300, Extron).
ii. The endoscopist inserted the spectral endoscope through the working channel of a therapeutic endoscope (GIF2T240, Olympus). The use of the therapeutic scope was required as the accessory channel was sufficiently large (3.7-mm diameter) to allow easy insertion of the spectral endoscope (3.0-mm diameter at tip, 2.65 mm along length). The spectral endoscope was used to inspect the regions of interest outlined in step i (**Fig. 2B**). An endoscope cap was not used as it can easily come into contact with lesions and induce contact bleeding, which can alter vascular pattern.
iii. The spectral endoscope was withdrawn and the endoscopist proceeded to an endoscopic mucosal resection or biopsy (depending on the endoscopic findings and the level of suspicion; **Fig. 2C**). Control areas received biopsies only. Pathological assessment of biopsies was performed by an expert GI pathologist with extensive experience in reporting Barrett's esophagus–related neoplasia (**Fig. 2D**; refs. 20–22). Histopathology was interpreted according to the revised Vienna classification (23). In case of dysplasia, a second pathologist reviewed the diagnosis to achieve consensus.

For analysis, the most advanced disease present in each biopsy determined the label for the region such that 3 classes of spectra were acquired: (i) Normal squamous; (ii) non-dysplastic Barrett's esophagus (NDBE) with and without intestinal metaplasia; (iii) neoplasia (consisting of dysplasia and intramucosal carcinoma). Crucially, this resulted in a set of *in vivo* tissue spectra labeled with gold standard diagnosis from histopathology for analysis.

Co-registration of spectral data with diagnosis from histopathology

To enable matching of spectral data with the diagnosis from histopathology, the SOC HR-WLE video stream and the video stream from the spectral endoscope were synchronized and placed side-by-side for analysis. The SOC video was carefully inspected to extract frames where the spectral endoscope was sampling the marked regions of interest that were biopsied to give gold standard diagnosis from histopathology. Frames were identified using the cautery marks and other visible landmarks in the HR-WLE video stream to estimate the field of view of the spectral endoscope, the tip of which was visible

Published OnlineFirst May 26, 2021; DOI: 10.1158/0008-5472.CAN-21-0474

Table 1. Summary of the collected spectral data and biopsies for matched regions.

Trial number	Barrett's Length (C = Circumferential, M = Maximum Extent)/cm	Location/cm	Location/ o'clock	Initial label during endoscopy	Tissue acquisition	Diagnosis from histopathology	Number of matched spectra
3	C0M2	37	8	Suspicious	EMR x 1	Barrett's	13
		37	4	Control	Biopsy x 1	Barrett's	9
4	C4M6	36	6	Control	Biopsy x 1	Barrett's	60
5	C5M7	31	9	Control	Biopsy x 1	Barrett's	28
6	C11M14	31	9	Control	Biopsy x 1	Barrett's	6
		28	6	Control	Biopsy x 1	Barrett's	9
7	C11M12	35	9	Control	Biopsy x 2	Barrett's	8
		32	5	Control	Biopsy x 2	Barrett's	7
8	C6M7	32	12	Control	Biopsy x 1	Barrett's	25
		30	6	Control	Biopsy x 1	Barrett's	4
9		34	3	Suspicious	EMR x 1	IMC	9
	C5M7	33	3	Suspicious	EMR x 1	IMC	16
		30	9	Control	Biopsy x 1	Barrett's	5
10	C14M14	32	10	Suspicious	Biopsy x 2	HGD	8
		24	10	Control	Biopsy x 1	Barrett's	7
11	C2M5	35	12	Suspicious	EMR x 1	HGD	7
		36	6	Control	Biopsy x 1	Barrett's	9
12	C2M4	41	6	Suspicious	EMR x 1	LGD	30
		39	8	Control	None	NA	5
		39	6	Control	Biopsy x 1	LGD	3
15	C3M4	35–38	9	Suspicious	EMR x 4	IMC	13
		37	3	Control	Biopsy x 1	Barrett's	8
16	C0M4	40	11	Suspicious	Biopsy x 1	IMC	7
		39	3	Control	Biopsy x 1	Barrett's	4
17	C0M2	37	1	Suspicious	Biopsy x 2	Barrett's	7
18	C5M7	26	12	Suspicious	EMR x 2	HGD	136
		25	9	Control	Biopsy x 1	Barrett's	106
		26	3	Suspicious	EMR x 1	HGD	7

Note: The number of matched spectra varies due to the imaging conditions. In some patients, finding frames where the endoscope interrogated the region of interest was more difficult due to poor visibility of the marking, peristaltic motion, or the position of the lesion within the esophagus.
Abbreviations: EMR, endoscopic mucosal resection; HGD, high-grade dysplasia; IMC, intramucosal carcinoma; LGD, low-grade dysplasia; NR, not reported.

within the HR-WLE field of view, allowing the selection of spectral data from tissue in precise correlation with gold standard diagnosis by histopathology.

Model-based spectral processing to determine vascular properties

Hemoglobin is the dominant tissue absorber in the visible and near-infrared range (5). Because oxyhemoglobin (HbO_2) and deoxyhemoglobin (Hb) have distinct absorption spectra, it is possible to determine oxygenation properties from tissue attenuation spectra (24). In addition, the spatial distribution of blood within the tissue affects the shape of the attenuation spectrum, allowing simple vessel characteristics to be extracted.

The absorption coefficient of whole blood is given by (24),

$$\mu_{a,bl}(\lambda) = 150 \cdot (\alpha \cdot \varepsilon_{Hb0_2}(\lambda) + (1-\alpha) \cdot \varepsilon_{Hb}(\lambda)) \cdot \frac{\ln 10}{64500} \ [\mathrm{cm}^{-1}], \quad (A)$$

where α [unitless] is the oxygen saturation, $\varepsilon_{Hb0_2}(\lambda)$ and $\varepsilon_{Hb}(\lambda)$ [$\mathrm{cm}^{-1}\mathrm{M}^{-1}$] are the molar extinction coefficients of HbO_2 and Hb, respectively, 64,500 g mol^{-1} is the molar mass of hemoglobin, and the hemoglobin concentration of whole blood is assumed to be 150 mg mL^{-1}. The ln 10 is used to convert from decadic to Napierian attenuation coefficient.

Typically, this is simplified to,

$$\mu_{a,bl}(\lambda) = \alpha \cdot \mu_{a,Hb0_2}(\lambda) + (1-\alpha) \cdot \mu_{a,Hb}(\lambda) \ [\mathrm{cm}^{-1}], \quad (B)$$

where $\mu_{a,Hb0_2}(\lambda)$ and $\mu_{a,Hb}(\lambda)$ [cm^{-1}] are the absorption coefficients of HbO_2 and Hb, respectively.

The measured tissue attenuation spectrum can be estimated as (25),

$$A(\lambda) = \langle L \rangle \cdot \nu \cdot C_{pack} \cdot \mu_{a,bl}(\lambda) \ [\text{unitless}], \quad (C)$$

where $\langle L \rangle$ [cm] is the average light path length through the tissue, ν [unitless] is the blood volume fraction and C_{pack} [unitless] is a vessel packing correction, which accounts for the inhomogeneous distribution of blood within tissue and is defined by,

$$C_{pack} = \frac{1 - \exp(-2 \cdot \mu_{a,bl}(\lambda) \cdot r_{vess})}{2 \cdot \mu_{a,bl}(\lambda) \cdot r_{vess}} \ [\text{unitless}], \quad (D)$$

where r_{vess} [cm] is the mean vessel radius over the volume sampled.

The combined effects of background scattering and additional sources of background absorption are approximated using a linear function, such that the total attenuation is modeled as,

$$A(\lambda) = \langle L \rangle \cdot \nu \cdot C_{pack} \cdot \mu_{a,bl}(\lambda) + k_0 + k_1 \cdot (\lambda - 500) \ [\text{unitless}], \quad (E)$$

where the coefficient k_0 [unitless] is not meaningful due to normalization, and the coefficient k_1 [unitless] describes the linear component

Published OnlineFirst May 26, 2021; DOI: 10.1158/0008-5472.CAN-21-0474

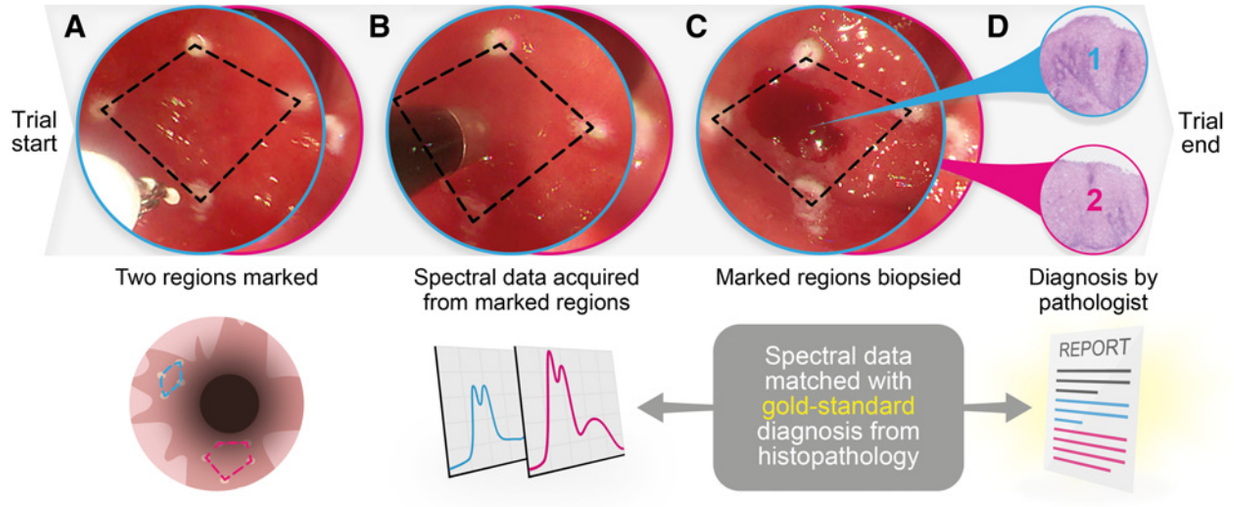

Figure 2.

Overview of the trial protocol. **A,** Two regions (dashed lines) are marked for inspection, one suspicious and one control, using cautery marking. **B,** Spectral data are acquired from each of the marked regions using the spectral endoscope. **C,** Following imaging, each of the marked regions is biopsied. **D,** These biopsies are assessed by a histopathologist to yield a gold standard diagnosis of each marked region. The spectral data are thus matched with a gold standard diagnosis.

of background attenuation. By fitting Eq. E to the acquired attenuation spectra using literature values (26) for $\mu_{a,Hb0_2}(\lambda)$ and $\mu_{a,Hb}(\lambda)$ [cm^{-1}], it is possible to extract α [unitless], the oxygen saturation, ν [unitless], the relative blood volume fraction (assuming similar measurement geometry $\langle L \rangle$), r_{vess} [cm], the mean vessel radius and k_1 [unitless], the linear component of background attenuation. For plotting, the relative blood volume fraction $\langle L \rangle$ is set to 1.

Learning-based spectral processing for classification

To test whether it is possible to use the measured attenuation spectra to classify tissues by disease type, a 1D convolutional neural network (CNN) model was trained (Supplementary Fig. S4). Attenuation spectra were randomly split 80:20 to train and test data, respectively. Training was performed for 500 epochs. No augmentation or pre-processing was applied to the data. For 3-way classification, the training data consisted of 572 spectra and the test data consisted of 143 spectra. For 2-way classification the number of spectra varied on the basis of the number of spectra present for each pathology.

Optimizing color channels for Barrett's esophagus surveillance

The acquired tissue spectra were used to simulate 3 imaging techniques: Two current clinical techniques, white-light imaging using 3 broad color filters and NBI using 2 narrow color filters; and one experimental, spectral imaging technique using 3 narrow color filters optimized for high-contrast imaging of neoplasia. For each of these techniques, images were simulated using the acquired tissue spectra, and the clinical techniques, WLE and NBI, were compared with spectral imaging to demonstrate the potential of the latter in high-contrast surveillance of Barrett's esophagus (Supplementary Methods).

Statistical analysis

Attenuation spectra per patient are presented as the mean ± standard error of all spectra acquired for each patient for each pathology, unless stated otherwise. Overall attenuation spectra are expressed as mean ± standard error of the mean attenuation spectra per patient, unless stated otherwise.

To examine sources of variance in the data, one-way ANOVA was performed to determine within-class and between-class variances (Supplementary Methods). Four root mean variances were quantified and compared: The intra-region variance (RMS_w^{region}) to characterize within-patient within-region heterogeneity (technical repeatability); the inter-region variance (RMS_b^{region}, only calculable where two distinct regions of the same class were measured within a patient) to characterize within-patient between-region heterogeneity (biological repeatability); intra-patient variance irrespective of region ($RMS_w^{patient}$); and the inter-patient variance ($RMS_b^{patient}$) to characterize between-patient heterogeneity (reproducibility). The root mean variance ratio $\sqrt{F}$, describing the ratio of between-group to within-group variance, was calculated to compare inter/intra-region heterogeneity ($\sqrt{F^{region}}$) and inter/intra-patient heterogeneity ($\sqrt{F^{patient}}$).

Because of the exploratory nature of this study and the absence of a previously acquired dataset, a formal calculation of sample size was not possible, so 20 patients (generating 40 regions) were set as a target for recruitment. Our relatively small dataset contains both paired and unpaired data, so a partially paired *t* test (not assuming equal variances; ref. 27) was used to assess pairwise differences between disease classes. It should be noted that this only allows for pairwise comparisons.

Results

Tissue attenuation spectra show promise for detecting neoplastic progression

We first computed the average attenuation spectra of different histopathological classes across all patients, which showed markedly different spectra according to disease status (**Fig. 3**). The peaks visible at 540 and 570 nm are characteristic of hemoglobin absorption and are significantly larger in the spectra of diseased tissue compared with those of healthy squamous tissue. In the spectra of NDBE and neoplasia, there is an apparent decrease in absorbance from 470 to

Published OnlineFirst May 26, 2021; DOI: 10.1158/0008-5472.CAN-21-0474

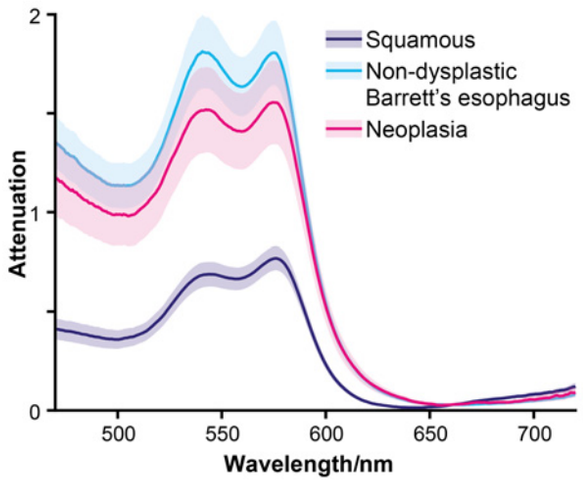

Figure 3.
Average attenuation spectra captured with the spectral endoscope across all patients. The shaded region represents the standard error across all patients (n = 715 spectra, n = 15 patients).

500 nm, potentially due to increased scattering in these disease phenotypes.

As expected, the collected spectra showed considerable heterogeneity between patients (Supplementary Fig. S5). To summarize this heterogeneity, measures of variance were calculated and compared (Supplementary Fig. S6A). Where spectra were available for distinct regions representing the same pathology within a single patient, a ratio of inter-region to intra-region variance, F^{region}, was calculated to characterize biological repeatability. This showed biological repeatability is higher in NDBE (mean $\sqrt{F^{region}} = 3.81$, range 1.17–7.02) compared with neoplasia (mean $\sqrt{F^{region}} = 9.33$, range 2.23–15.31), suggesting increased heterogeneity in more advanced disease (Supplementary Fig. S6B). Similarly, the inter-patient variance increases with disease progression ($RMS_b^{patient} = 0.42$ vs. 1.29 vs. 1.62 for squamous, NDBE and neoplasia, respectively), suggesting increased heterogeneity in tissue optical properties for more advanced disease (Supplementary Fig. S6C). A ratio of inter-patient to intra-patient variance, $F^{patient}$, was calculated to determine reproducibility. For all pathologies $F^{patient} \gg 1$ ($\sqrt{F^{patient}} = 4.61$, 6.32, 8.79 for squamous, NDBE and neoplasia, respectively), that is, the inter-patient variance is large in comparison with the intra-patient variance, thus presenting a challenge for a global classification across patients (Supplementary Fig. S6D). Still, spectral differences are conserved between classes within each patient, suggesting a contextual classification method would more likely be successful.

Tissue vascular properties change with disease status

To quantify vascular properties, a model of blood attenuation that accounts for both vascular oxygen saturation and vessel radius (**Fig. 4A**) was fitted to the acquired attenuation spectra per-patient (**Fig. 4B**; mean root mean squared error = 0.023, n = 30). Oxygen saturation remained constant across the tissue types studied (**Fig. 4C**). Vessel radius was found to be decreased in NDBE compared with squamous tissue (t = 2.87, df = 11.1, P = 0.008) and neoplasia (t = −1.73, df = 8.46, P = 0.06; **Fig. 4D**). Relative blood volume fraction was found to be increased in NDBE and neoplasia relative to healthy squamous tissue (t = −3.87, df = 11.1, P = 0.001 and t = −2.62, df = 5.44, P = 0.02, respectively; **Fig. 4E**). Significant differences in the linear background attenuation were observed between all three classes (**Fig. 4F**).

Deep-learning enables classification of tissue types

To test whether it is possible to use the measured attenuation spectra to classify tissues by disease type, a 1D CNN model was trained (Supplementary Fig. S3). A t-distributed stochastic neighbor-embedding visualization of train (Supplementary Fig. S7A) and test (Supplementary Fig. S7B) samples for 3-way classification leads to predicted probability from our trained CNN model (Supplementary Fig. S7C). Both 3-way classification, to classify squamous tissue, NDBE, and neoplasia, and 2-way classification, to classify each pair of tissue pathologies, were performed. Notably, 2-way classification between NDBE and neoplasia is most relevant to the clinical challenge in Barrett's esophagus surveillance, where neoplasia is often inconspicuous within a large area of NDBE.

The 1D CNN achieved high accuracy for classification of attenuation spectra (n = 143) both in 3-way classification and in 2-way classification, with a test-time per-spectrum of <0.001 ms (**Table 2**). Classification was also performed using k-nearest-neighbors and support-vector machine algorithms, but these performed with inferior accuracy to the CNN (Supplementary Tables S2 and S3). Notably with respect to the relevant clinical problem, the detection of neoplasia in NDBE, the 1D CNN achieved 84.8% accuracy, with 83.7% sensitivity, 85.5% specificity, 78.3% positive predictive value, and 89.4% negative predictive value. Performance on training data is shown in Supplementary Tables S4 and S5.

Spectra from patients 4 and 18 are overrepresented in the dataset [**Table 1**; mean (standard deviation) spectra per region = 19.3 (27.6); patient 4, NDBE spectra n = 60; patient 18, first neoplastic region spectra n = 136 and NDBE spectra n = 106]. To balance the dataset, 12 spectra were randomly selected from each of these 3 regions. Results from classification of this balanced dataset are shown in Supplementary Tables S6–S8 for CNN, k-nearest-neighbors and support-vector machine algorithms, respectively. This balancing had little effect on the overall accuracy of 3-way CNN-based classification but slightly decreased the accuracy of 2-way CNN-based classification of neoplasia versus NDBE (72.4% vs. 84.8%).

Optimizing color channels for Barrett's esophagus surveillance could enhance clinical contrast for neoplasia

We exploited our acquired library of labeled tissue spectra to systematically determine a set of narrow band filters tailored to high-contrast imaging of neoplasia in Barrett's esophagus that could be deployed clinically. To do this, the measured reflectance spectra were propagated through simulated filter sets for 3 imaging techniques: Two current clinical techniques, namely white-light imaging using 3 broad color filters and NBI using 2 narrow color filters; and a new multispectral imaging set using 3 narrow color filters optimized for high-contrast imaging of neoplasia (Supplementary Methods).

To simulate WLE and NBI images, the known color filters deployed in SOC endoscopes were used to simulate images (Supplementary Fig. S8A). To simulate spectral imaging, three-color filters (Supplementary Fig. S8B) were selected to optimize contrast for neoplasia on a standard red–green–blue (RGB) color display that would be found in endoscopy suites. Briefly, the acquired spectra were processed to yield reflection spectra; next, the detection of these reflection spectra by narrow color filters with a range of center wavelengths (490–720 nm in steps of 10 nm) and sensitivities

Published OnlineFirst May 26, 2021; DOI: 10.1158/0008-5472.CAN-21-0474

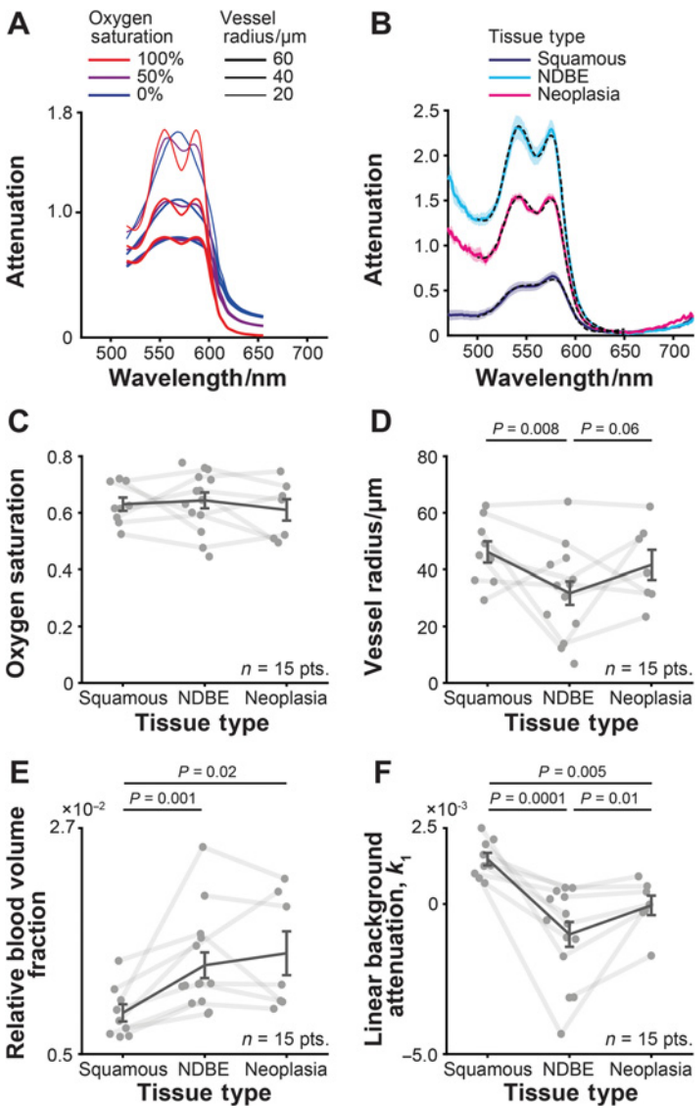

Figure 4.

Vascular and oxygenation characteristics derived from fits to acquired attenuation spectra. **A,** Example attenuation spectra generated by the blood attenuation model illustrated for three different oxygen saturation levels and three different vessel radii (Eq. E, $\langle L \rangle = 1$, $v = 0.01$, $k_0 = 0$, $k_1 = 0$). **B,** The blood attenuation model was fitted to the mean attenuation spectra per patient per pathology. An example of this (dotted line) is shown for patient 11. The shaded region represents the standard error in spectra within this patient. **C–F,** The values of the fit coefficients are shown for oxygen saturation (**C**), mean vessel radius (**D**), relative blood volume fraction (**E**), and linear background attenuation (**F**). Trends within each patient are highlighted with solid gray lines. Solid black lines represent the average over all patients ± SE. *P* values were calculated using the partially paired *t* test (27). NDBE, non-dysplastic Barrett's esophagus. $n = 15$ patients.

Table 2. Performance of CNN classification of tissue attenuation spectra.

	Classification performance				
Comparison	**Accuracy (%; *n*/total)**	**Sensitivity (%; *n*/total)**	**Specificity (%; *n*/total)**	**Positive predictive value (%; *n*/total)**	**Negative predicative value (%; *n*/total)**
3-way classification					
Squamous	98.6 (141/143)	100.0 (22/22)	98.3 (119/121)	91.7 (22/24)	100.0 (119/119)
NDBE	87.4 (125/143)	92.1 (58/63)	83.8 (67/80)	81.7 (58/71)	93.1 (67/72)
Neoplasia	87.4 (125/143)	75.9 (44/58)	95.3 (81/85)	91.7 (44/48)	85.3 (81/95)
2-way Classification[a]					
NDBE vs. squamous	97.9 (94/96)	98.3 (59/60)	97.2 (35/36)	98.3 (59/60)	97.2 (35/36)
Neoplasia vs. squamous	98.7 (78/79)	100.0 (48/48)	96.8 (30/31)	98.0 (48/49)	100.0 (30/30)
Neoplasia vs. NDBE	84.8 (95/112)	83.7 (36/43)	85.5 (59/69)	78.3 (36/46)	89.4 (59/66)

Abbreviation: NDBE, non-dysplastic Barrett's esophagus.

[a]In 2-way comparisons, the class in italics is the target for purposes of classification performance metric.

Published OnlineFirst May 26, 2021; DOI: 10.1158/0008-5472.CAN-21-0474

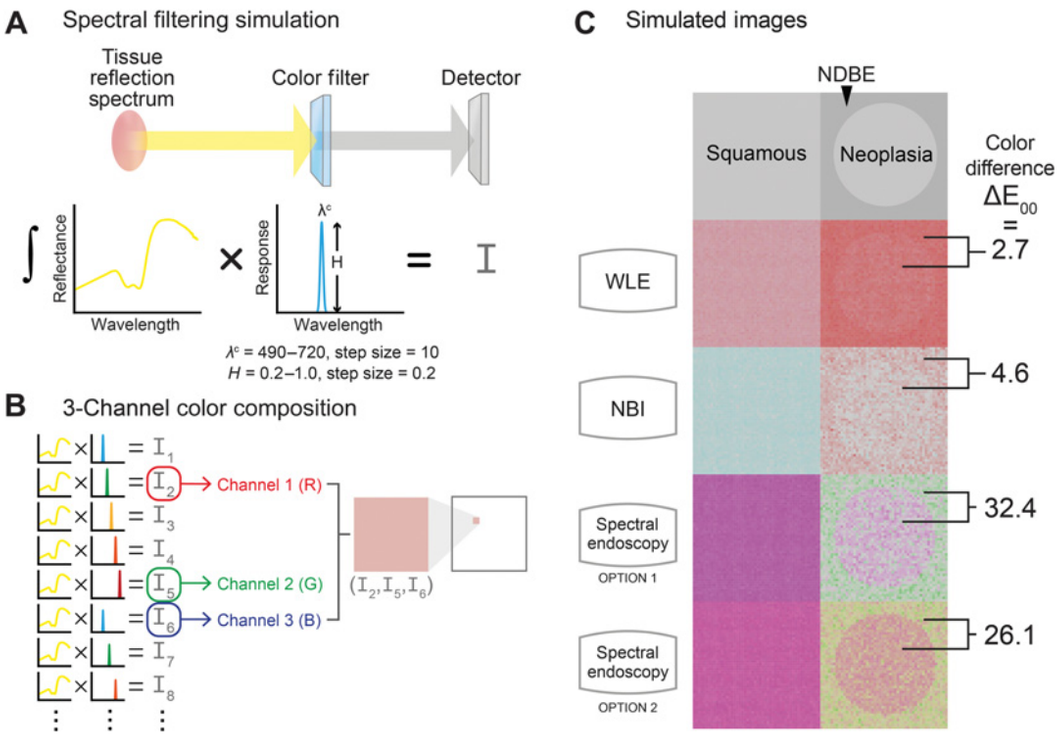

Figure 5.

Simulated images comparing neoplasia with NDBE and squamous tissue. **A,** Schematic representation of the process for simulating the propagation of a tissue reflectance spectrum through a color filter to calculate a detected intensity, I. This process is repeated for a range of narrow band color filters (center wavelengths 490–720 nm, step size = 10 nm; sensitivities 0.2–1.0, step size = 10, arbitrary units). **B,** For every combination of three simulated color filters, a 3-channel color is composed by assigning the three simulated intensities to the red, green, and blue image channels, thus generating a color pixel. The combination of three simulated color filters that maximizes the International Commission on Illumination Delta E 2000 (CIEDE2000) color difference (ΔE_{00}) between NDBE and neoplasia is chosen as spectral endoscopy filter set option 1. **C,** Using this filter set, the process of color filtering and color composition is repeated pixel-by-pixel to generate simulated images. For comparison, images are also simulated using white-light endoscopy (WLE) and narrow band imaging (NBI) filter sets. Images simulated using a second optimized spectral endoscopy filter set (option 2), determined as a distinct set that second-most enhanced CIEDE2000 color difference between NDBE and neoplasia, are also shown. The mean CIEDE2000 color difference (ΔE_{00}) between neoplasia and NDBE is shown for the images simulated using the four filter sets. The mean CIEDE2000 color differences between squamous and NDBE were 14.4, 23.4, 53.0, and 52.5 for WLE, NBI, and spectral endoscopy options 1 and 2, respectively.

(0.2–1.0 in steps of 0.2 arbitrary units) was simulated (**Fig. 5A**); finally, the detected signal intensities from 3 of the narrow color filters were selected to display on the RGB channels of standard display equipment, thus defining the observed color (**Fig. 5B**). The combination of narrow color filters that achieved the largest color difference between NDBE and neoplasia according to the International Commission on Illumination Delta E 2000 (CIEDE2000) color difference (ΔE_{00}; ref. 28) was selected for comparison with SOC.

Simulated HR-WLE and NBI match the characteristic pink/red and greenish–blue/burgundy–gray colors observed in SOC imaging, suggesting that the approach used to simulate images from acquired spectra can appropriately represent the existing spectral approaches used in endoscopy (**Fig. 5C**). Note, the NBI images of NDBE and neoplasia appear lighter compared with their typical appearance on endoscopic evaluation, because the displayed images are normalized to display chromaticity (color independent of brightness), but the red pixels are suggestive of NBI's vascular imaging capabilities. In both WLE and NBI, there is low contrast for neoplasia in NDBE, as expected given the current clinical challenge (color difference, $\Delta E_{00} = 2.7$ and 4.6, respectively).

The results of the color difference optimization for spectral endoscopy using only 3 narrow band color filters produced a strong purple/green color contrast in one configuration and a strong pink/yellow contrast in a second, alternative combination (**Fig. 5C**). With spectral endoscopy optimized using the acquired spectra, neoplasia would be clearly distinguishable (color difference, $\Delta E_{00} = 32.4$, a 12-fold increase vs. SOC HR-WLE), demonstrating untapped potential for using custom color filters in endoscopy to increase contrast in surveillance of Barrett's esophagus.

Discussion

Barrett's esophagus–related neoplasia, if detected early, is curable using minimally invasive endoscopic therapy, but it is challenging to identify due to limited contrast on SOC endoscopic imaging (2, 3). Advanced endoscopic imaging techniques that increase contrast by acquiring additional optical information from tissue are key to improving upon the SOC (4). One promising approach is to acquire additional spectral information (6, 7). The development of NBI over the past 15 years represents a successful step in this direction, and showcases the advantage of spectral imaging techniques (13). We

hypothesized that spectral endoscopy could enhance contrast for neoplasia in surveillance of patients with Barrett's esophagus.

To test this hypothesis, we conducted a pilot clinical study using a custom spectral endoscope to acquire spectra that were precisely matched with a histopathological diagnosis. Our methodology emphasized accurate collection of matched spectral data and biopsies to ensure that the acquired spectra were reliably labeled with a gold standard histopathological diagnosis. The importance of gold standard diagnosis is evident in cases misdiagnosed on endoscopy (**Table 1**); of the 28 regions of NDBE and neoplasia biopsied, 2 regions considered suspicious on endoscopy were diagnosed as NDBE and 1 region considered to be a control on endoscopy was diagnosed as low-grade dysplasia, despite expert assessment. The discrepancy between endoscopic and pathological diagnosis can be significantly higher when surveillance endoscopies are performed without image-enhanced techniques or by endoscopists with less experience in early detection of Barrett's esophagus–related neoplasia (29).

The trial resulted in a total of approximately 77 minutes of video (5.2 ± 1.5 minutes per trial) corresponding to approximately 18,000 spectra ($1{,}200 \pm 400$ spectra per patient). These videos were thoroughly inspected to extract frames where the spectral endoscope was sampling the marked regions of interest. The result was a labeled dataset of 556 spectra from NDBE or neoplasia and 159 spectra from endoscopically normal squamous tissue.

The acquired attenuation spectra were fit to a model of blood attenuation to reveal underlying changes in vasculature in the progression of disease. Diffusely reflected light collected in our spectral endoscope is estimated to penetrate approximately 200 ± 100 μm into tissue (11), thus sampling the superficial mucosal layers where angiogenesis occurs in disease progression. As new microvessels form from the pre-existing vascular network in the lamina propria, they infiltrate the epithelium (30). The observed decrease in mean vessel radius between squamous tissue and NDBE is consistent with the formation of these new microvessels (vessels of small radius). The observed increase in mean vessel radius between NDBE and neoplasia is suggestive of vessel maturation and/or inflammation during later stages of neoplastic progression. Furthermore, relative blood volume fraction was increased in NDBE and neoplasia relative to healthy squamous tissue, consistent with early neovascularization in Barrett's esophagus (30–38). Although these changes in the microvasculature can be qualitatively assessed on NBI with magnification or near focus, the interpretation of the vascular pattern can be subjective and in 40%–50% of cases the diagnosis is made with low level of confidence, even by expert endoscopists (39). Therefore, the ability to quantify these parameters more objectively afforded by spectral endoscopy could be a significant aid to interpretation and hence diagnostic capability.

The oxygen saturation showed no significant changes between tissue types and was around 65%, consistent with previously reported levels (40). The pathological relevance of this finding is unclear, because prior literature reports considering vascularization and hypoxia in the esophagus are conflicting. For example, Griffiths and colleagues (38) observed a decrease in hypoxia markers from squamous epithelium to NDBE, whereas Ling and colleagues (41) observed the opposite effect. Several of the commonly used markers are also associated with inflammation, an almost ubiquitous feature of NDBE, hence the interpretation of these data is challenging. In addition, many of the neoplastic lesions imaged in this trial were early stage, so dramatic changes in the level of oxygenation are not expected.

Significant differences in the linear background attenuation were observed between all three classes. This fitted term represents the combined effects of background scattering and additional sources of background absorption, so represents a mixture of different structural and functional changes that occur in the tissue. Still, the significant differences between classes, particularly between NDBE and neoplasia suggest that this might be a useful metric for classification, albeit with future validation required.

Classification of the acquired attenuation spectra using a CNN-achieved high accuracy. Notably, the relevant clinical challenge of differentiating between NDBE and neoplasia was possible with 84.8% accuracy (95/112 spectra classified correctly). Our results compare favorably with prior literature: Douplik and colleagues (16) achieved similar classification performance using linear discriminant analysis to classify dysplastic spectra with 77% sensitivity and 86% specificity when averaging 20–30 sequential spectra per region; Georgakoudi and colleagues (14) achieved 79% sensitivity and 88% specificity for classifying dysplastic tissue using logistic regression, but their analysis relied on leave-one-out cross validation owing to their small sample size; furthermore, Bergholt and colleagues (42) achieved a sensitivity of 87.0% and a specificity of 84.7% using vibrational Raman spectroscopy.

Though our findings are promising, the small dataset collected in this trial limited our performance characterization to a per-spectra analysis with a random 80:20 split into training and test set. The performance characteristics of our classification are already close to the minimum sensitivity and specificity thresholds required by the American Society for Gastrointestinal Endoscopy PIVI standards (12), suggesting that the potential for future clinical impact with further enrichment of the dataset. Future work with a larger dataset should employ a per-patient split on a dedicated test set to assess the CNN's performance when dealing with unseen patients, particularly in light of the large inter-patient variation seen in this trial.

The results emerging from our spectral endoscopy data are promising to aid interpretation of existing NBI data and for classification of tissue type; however, the use of a babyscope to acquire such data extends procedure time and, more importantly, relies on an accurate wide-field imaging method to identify suspicious regions for interrogation with spectroscopy. As noted, the contrast for early neoplastic change afforded by WLE and NBI remains limited. We therefore asked whether it would be possible to optimize a custom color filter set to obtain contrast enhancement using alternative spectral bands to those currently found in clinical practice. The resulting simulated images demonstrate vastly improved contrast for the spectral endoscope compared with NBI and WLE (color difference, $\Delta E_{00} = 32.4$ vs. 4.6 vs. 2.7, respectively), advocating the technological development of endoscopes with application-specific color filter sets. Notably, these results are independent of the hardware configuration chosen to achieve the combination of color filters (e.g., filter wheel, spectrally resolved detector array, etc.). Future work could further expand this analysis to >3 color filters given the recent emergence of nanofabrication methods that enable facile fabrication of multispectral imaging cameras (43).

Despite these overall promising findings, our study has several limitations. First, though exhaustive effort was undertaken to accurately match spectral data with histopathology, the disease is spatially heterogeneous, even at small scales (<1 mm). In regions with diagnosis of multifocal disease, it is likely that some acquired spectra include contributions from both focal neoplasia and the surrounding "sea" of NDBE. On the one hand this is positive, it suggests that our acquired neoplastic spectra are diluted by the inclusion of NDBE contributions, hence contrast is likely to be greater than measured here. Unfortunately, it also inevitably means that acquiring "pure" ground truth spectra *in vivo* is likely to be impossible in this disease setting. This was

Published OnlineFirst May 26, 2021; DOI: 10.1158/0008-5472.CAN-21-0474

particularly affected by the inclusion of patients with early neoplastic disease, which represent the main clinical challenge in routine diagnostics. Future work to achieve optimized color imaging at high resolution might mitigate this challenge by allowing tissue heterogeneity to be spatially resolved. Nonetheless, as image segmentation becomes more detailed, so the co-registration of the image field with histopathology becomes more challenging. Careful consideration of these issues should be made in future studies aiming to use advanced spectral endoscopy methods to aid in Barrett's esophagus surveillance.

Second, the current study relied on an imaging fiber bundle to carry light to detectors outside the body, resulting in a single-point spectrum per frame. Spatial (image) information is critically important in Barrett's esophagus surveillance; the success of NBI relies on its combination of both high contrast and spatial resolution to reveal diagnostically useful image features, such as blood vessels and pit patterns. Optimized, application-specific, color filter sets could be applied clinically in a standard chip-on-tip endoscope architecture, by a simple modification of either the illumination light source or by the introduction of a custom color camera at the endoscope tip (44, 45). New methods of optical filter fabrication (43, 46) increasingly allow for cost-effective manufacture of custom cameras that would be appropriate for such a task. The labeled disease spectra acquired in this study facilitate, for the first time, a systematic approach to optimizing such filter sets and demonstrating the feasibility of using our optimized color channels for imaging, rather than simply point sensing as implemented here, is an important aspect of future work.

In conclusion, we have demonstrated the potential of spectral endoscopy to improve contrast in surveillance of Barrett's esophagus. In particular, using model-based analysis we show that spectral endoscopy is able to reveal the vascular characteristics of esophageal tissue during neoplastic progression. Furthermore, combining spectral endoscopy with learning-based analysis we found that the attenuation spectra could distinguish between tissue pathologies with high accuracy. With optimized selection of color filters, spectral endoscopy has the potential to provide high contrast for neoplasia during surveillance of Barrett's esophagus, thus addressing a long-standing clinical challenge.

Authors' Disclosures

D.J. Waterhouse reports a patent for determination of spectral filters for spectral imaging pending. R.C. Fitzgerald reports other support from Medtronic and CYTED outside the submitted work. S.E. Bohndiek reports grants from Cancer Research UK and EPSRC during the conduct of the study, as well as grants from PreXion Inc. (CYBERDYNE) outside the submitted work, and reports patent for determination of spectral filters for spectral imaging pending. No disclosures were reported by the other authors.

Authors' Contributions

D.J. Waterhouse: Conceptualization, data curation, software, formal analysis, investigation, methodology, writing–original draft, writing–review and editing. **W. Januszewicz:** Investigation, writing–review and editing. **S. Ali:** Software, formal analysis, methodology. **R.C. Fitzgerald:** Conceptualization, funding acquisition, methodology, writing–review and editing. **M. di Pietro:** Conceptualization, supervision, funding acquisition, investigation, methodology, writing–review and editing. **S.E. Bohndiek:** Conceptualization, resources, supervision, funding acquisition, methodology, writing–original draft, project administration, writing–review and editing.

Acknowledgments

D.J. Waterhouse received an EPSRC Doctoral Fellowship. R.C. Fitzgerald and S.E. Bohndiek received a CRUK Multidisciplinary Project Award (C47594/A21102). S.E. Bohndiek received a CRUK Career Establishment Award (C47594/A16267), Core Funding (C14303/A17197, C9545/A29580), Pioneer Award (C55962/A24669), and an EPSRC Healthcare Technologies Challenge Award (EP/R003599/1). This work was supported in part by the EPSRC Center for Mathematical Imaging in Healthcare (EP/N014588/1), the National Institute of Cancer Research, and the infrastructure support from the Experimental Cancer Imaging Center and Cambridge Biomedical Research Center. This study would not have been possible without hard work of the staff of the Cambridge Clinical Research Center. Many thanks to Tara Evans for her help in recruitment for this study. The authors would also like to thank Maria O'Donovan for her work in histopathology. The authors would like to express our deepest gratitude to those patients who agreed to take part in this study, without whom this research would not have been possible.

The costs of publication of this article were defrayed in part by the payment of page charges. This article must therefore be hereby marked *advertisement* in accordance with 18 U.S.C. Section 1734 solely to indicate this fact.

Received February 10, 2021; revised April 1, 2021; accepted April 16, 2021; published first May 26, 2021.

References

1. Gatenby P, Caygill C, Wall C, Bhatacharjee S, Ramus J, Watson A, et al. Lifetime risk of esophageal adenocarcinoma in patients with Barrett's esophagus. World J Gastroenterol 2014;20:9611–7.
2. Spechler SJ, Sharma P, Souza RF, Inadomi JM, Shaheen NJ. American Gastroenterological Association technical review on the management of Barrett's esophagus. Gastroenterology 2011;140:e18–52.
3. Fitzgerald RC, di Pietro M, Ragunath K, Ang Y, Kang J-Y, Watson P, et al. British society of gastroenterology guidelines on the diagnosis and management of Barrett's oesophagus. Gut 2014;63:7–42.
4. Waterhouse DJ, Fitzpatrick CRM, di Pietro M, Bohndiek SE. Emerging optical methods for endoscopic surveillance of Barrett's oesophagus. Lancet Gastroenterol Hepatol. Elsevier Ltd. 2018;3:349–62.
5. Bigio IJ, Fantini S. Quantitative Biomedical Optics. Cambridge, UK: Cambridge University Press; 2016.
6. Lu G, Fei B. Medical hyperspectral imaging: a review. J Biomed Opt 2014;19:10901.
7. Calin MA, Parasca SV, Savastru D, Manea D. Hyperspectral imaging in the medical field: present and future. Appl Spectrosc Rev 2014;49:435–47.
8. Imamoto Y, Shichida Y. Cone visual pigments. Biochim Biophys Acta. 2014;1837:664–73.
9. Gono K. Narrow band imaging: technology basis and research and development history. Clin Endosc 2015;48:476–80.
10. de Groof AJ, Swager A-F, Pouw RE, Weusten BLAM, Schoon EJ, Bisschops R, et al. Blue-light imaging has an additional value to white-light endoscopy in visualization of early Barrett's neoplasia: an international multicenter cohort study. Gastrointest Endosc. 2019;89:749–58.
11. Gono K, Obi T, Yamaguchi M, Ohyama N, Machida H, Sano Y, et al. Appearance of enhanced tissue features in narrow-band endoscopic imaging. J Biomed Opt 2004;9:568–77.
12. Sharma P, Savides TJ, Canto MI, Corley D a, Falk GW, Goldblum JR, et al. The American Society for Gastrointestinal Endoscopy PIVI (Preservation and Incorporation of Valuable Endoscopic Innovations) on imaging in Barrett's Esophagus. Gastrointest Endosc 2012;76:252–4.
13. Thosani N, Abu Dayyeh BK, Sharma P, Aslanian HR, Enestvedt BK, Komanduri S, et al. ASGE Technology Committee systematic review and meta-analysis assessing the ASGE Preservation and Incorporation of Valuable Endoscopic Innovations thresholds for adopting real-time imaging–assisted endoscopic targeted biopsy during endoscopic surveillance. Gastrointest Endosc 2016;83:684–98.
14. Georgakoudi I, Jacobson BC, Dam JVAN, Backman V, Wallace MB, Mu MG, et al. Fluorescence, reflectance, and light-scattering spectroscopy for evaluating dysplasia in patients with Barrett's esophagus. Gastroenterology 2001;120:1620–9.
15. Qiu L, Pleskow DK, Chuttani R, Vitkin E, Leyden J, Ozden N, et al. Multispectral scanning during endoscopy guides biopsy of dysplasia in Barrett's esophagus. Nat Med 2010;16:603–6.
16. Douplik A, Zanati S, Saiko G, Streutker C, Loshchenov M, Adler D, et al. Diffuse reflectance spectroscopy in Barrett's esophagus: developing a large field-of-view

screening method discriminating dysplasia from metaplasia. J Biophotonics 2014;7:304–11.
17. Georgakoudi I, Feld MS. The combined use of fluorescence, reflectance, and light-scattering spectroscopy for evaluating dysplasia in Barrett's esophagus. Gastrointest Endosc Clin N Am 2004;14:519–37.
18. Qiu L, Chuttani R, Pleskow DK, Turzhitsky V, Khan U, Zakharov YN, et al. Multispectral light scattering endoscopic imaging of esophageal precancer. Light Sci Appl. 2018;7:17174.
19. Sharma P, Dent J, Armstrong D, Bergman JJGHM, Gossner L, Hoshihara Y, et al. The development and validation of an endoscopic grading system for Barrett's esophagus: the Prague C & M Criteria. Gastroenterology 2006;131:1392–9.
20. Bird-Lieberman EL, Neves AA, Lao-Sirieix P, O'Donovan M, Novelli M, Lovat LB, et al. Molecular imaging using fluorescent lectins permits rapid endoscopic identification of dysplasia in Barrett's esophagus. Nat Med 2012;18:315–21.
21. Neves AA, PM Di, Donovan MO, Waterhouse DJ, Bohndiek SE, Brindle KM, et al. Detection of early neoplasia in Barrett's esophagus using lectin-based near-infrared imaging: an *ex vivo* study on human tissue. Endoscopy 2018;50:618–25.
22. di Pietro M, Boerwinkel DF, Shariff MK, Liu X, Telakis E, Lao-Sirieix P, et al. The combination of autofluorescence endoscopy and molecular biomarkers is a novel diagnostic tool for dysplasia in Barrett's oesophagus. Gut 2015;64:49–56.
23. Dixon MF. Gastrointestinal epithelial neoplasia: Vienna revisited. Gut 2002;51:130–1.
24. Stratonnikov AA, Loschenov VB. Evaluation of blood oxygen saturation *in vivo* from diffuse reflectance spectra. J Biomed Opt 2001;6:457–67.
25. van Veen RLP, Verkruysse W, Sterenborg HJCM. Diffuse-reflectance spectroscopy from 500 to 1060 nm by correction for inhomogeneously distributed absorbers. Opt Lett 2002;27:246–8.
26. Bosschaart N, Edelman GJ, Aalders MCG, Van Leeuwen TG, Faber DJ. A literature review and novel theoretical approach on the optical properties of whole blood. Lasers Med Sci 2014;29:453–79.
27. Derrick B, Toher D, White P. How to compare the means of two samples that include paired observations and independent observations: a companion to Derrick, Russ, Toher and White (2017). Quant Methods Psychol 2017;13:120–6.
28. Luo MR, Cui G, Rigg B. The development of the CIE 2000 colour-difference formula: CIEDE2000. Color Res Appl 2001;26:340–50.
29. Tholoor S, Bhattacharyya R, Tsagkournis O, Longcroft-Wheaton G, Bhandari P. Acetic acid chromoendoscopy in Barrett's esophagus surveillance is superior to the standardized random biopsy protocol: results from a large cohort study (with video). Gastrointest Endosc 2014;80:417–24.
30. Auvinen MI, Sihvo EIT, Ruohtula T, Salminen JT, Koivistoinen A, Siivola P, et al. Incipient angiogenesis in Barrett's epithelium and lymphangiogenesis in Barrett's adenocarcinoma. J Clin Oncol 2002;20:2971–9.
31. Picardo SL, Maher SG, O'Sullivan JN, Reynolds JV. Barrett's to oesophageal cancer sequence: a model of inflammatory-driven upper gastrointestinal cancer. Dig Surg 2012;29:251–60.
32. Morales CP, Souza RF, Spechler SJ. Hallmarks of cancer progression in Barrett's oesophagus. Lancet 2002;360:1587–9.
33. Möbius C, Stein HJ, Becker I, Feith M, Theisen J, Gais P, et al. The "angiogenic switch" in the progression from Barrett's metaphasia to esophageal adenocarcinoma. Eur J Surg Oncol 2003;29:890–4.
34. Lord RVN, Park JM, Wickramasinghe K, DeMeester SR, Oberg S, Salonga D, et al. Vascular endothelial growth factor and basic fibroblast growth factor expression in esophageal adenocarcinoma and Barrett esophagus. J Thorac Cardiovasc Surg 2003;125:246–53.
35. Konda VJA, Hart J, Lin S, Tretiakova M, Gordon IO, Campbell L, et al. Evaluation of microvascular density in Barrett's associated neoplasia. Mod Pathol 2013;26:125–30.
36. Couvelard A, Paraf F, Gratio V, Scoazec JY, Hénin D, Degott C, et al. Angiogenesis in the neoplastic sequence of Barrett's oesophagus. Correlation with VEGF expression. J Pathol 2000;192:14–8.
37. Saad RS, El-Gohary Y, Memari E, Liu YL, Silverman JF. Endoglin (CD105) and vascular endothelial growth factor as prognostic markers in esophageal adenocarcinoma. Hum Pathol 2005;36:955–61.
38. Griffiths EA, Pritchard SA, McGrath SM, Valentine HR, Price PM, Welch IM, et al. Increasing expression of hypoxia-inducible proteins in the Barrett's metaplasia-dysplasia-adenocarcinoma sequence. Br J Cancer 2007;96:1377–83.
39. Sharma P, Bergman JJGHM, Goda K, Kato M, Messmann H, Alsop BR, et al. Development and validation of a classification system to identify high-grade dysplasia and esophageal adenocarcinoma in Barrett's esophagus using narrow band imaging. Gastroenterology 2016;150:591–8.
40. Ueda S, Saeki T, Osaki A, Yamane T, Kuji I. Bevacizumab induces acute hypoxia and cancer progression in patients with refractory breast cancer: Multimodal functional imaging and multiplex cytokine analysis. Clin Cancer Res 2017;23:5769–78.
41. Ling FC, Khochfar J, Baldus SE, Brabender J, Drebber U, Bollschweiler E, et al. HIF-1α protein expression is associated with the environmental inflammatory reaction in Barrett's metaplasia. Dis Esophagus 2009;22:694–9.
42. Bergholt MS, Zheng W, Ho KY, Teh M, Yeoh KG, Yan So JB, et al. Fiberoptic confocal raman spectroscopy for real-time *in vivo* diagnosis of dysplasia in Barrett's esophagus. Gastroenterology 2014;146:27–32.
43. Williams C, Gordon GSD, Wilkinson TD, Bohndiek SE. Grayscale-to-color: scalable fabrication of custom multispectral filter arrays. ACS Photonics 2019;6:3132–41.
44. Lapray PJ, Wang X, Thomas JB, Gouton P. Multispectral filter arrays: Recent advances and practical implementation. Sensors 2014;14:21626–59.
45. Saxe S, Sun L, Smith V, Meysing D, Hsiung C, Houck A, et al. Advances in miniaturized spectral sensors. Proc SPIE 2018;10657:106570B.
46. Chen Q, Hu X, Wen L, Yu Y, Cumming DRS. Nanophotonic image sensors. Small. 2016;12:4922–35.

Published OnlineFirst May 26, 2021; DOI: 10.1158/0008-5472.CAN-21-0474

Cancer Research
The Journal of Cancer Research (1916–1930) | The American Journal of Cancer (1931–1940)

AACR American Association for Cancer Research

Spectral Endoscopy Enhances Contrast for Neoplasia in Surveillance of Barrett's Esophagus

Dale J. Waterhouse, Wladyslaw Januszewicz, Sharib Ali, et al.

Cancer Res 2021;81:3415-3425. Published OnlineFirst May 26, 2021.